Elasticity of single-crystalline graphite: Inelastic x-ray scattering study

Alexey Bosak and Michael Krisch
European Synchrotron Radiation Facility, BP 220, F-38043 Grenoble Cedex, France

Marcel Mohr, Janina Maultzsch, and Christian Thomsen
Institut für Festkörperphysik, Technische Universität Berlin, Hardenbergstrasse 36, 10623 Berlin, Germany
(Received 22 November 2006; revised manuscript received 11 January 2007; published 30 April 2007)

The five independent elastic moduli of single-crystalline graphite are determined using inelastic x-ray scattering. At room temperature the elastic moduli are, in units of GPa, $C_{11}=1109$, $C_{12}=139$, $C_{13}=0$, $C_{33}=38.7$, and $C_{44}=4.95$. Our experimental results are compared with predictions of *ab initio* calculations and previously reported incomplete and contradictory data sets. We obtain an upper limit of 1.1 TPa for the on-axis Young's modulus of homogeneous carbon nanotube, thus providing important constraints for further theoretical advances and quantitative input to model elasticity in graphite nanotubes.

DOI: 10.1103/PhysRevB.75.153408 PACS number(s): 61.10.Eq, 63.20.Dj, 62.20.Dc

Graphite is one of the very few elemental solids for which a comprehensive and complete determination of its elastic properties is still missing. This is surprising in view of the important role played by graphite in various technological applications—for example, as dry lubricant, as moderator in nuclear power plants, in medical surgery, and as very strong and heat-resistant carbon fiber. Further interest in carbon was sparked by the discovery and controlled synthesis of nanotubes[1] and their potential in applications, exploiting their exceptional mechanical properties. Furthermore, the recent realization of graphene-based (one-atom-thick two-dimensional layers of sp^2-bonded carbon) composite materials promises novel applications in microelectronics.[2] The lack of complete and reliable data for its elastic properties is, on the one hand, due to the unavailability of sufficiently large single crystals, which make the application of classical experimental techniques, such as ultrasound measurements, impossible, and on the other hand, due to the large spread among computational results.

The experimental determination of the elastic moduli constitutes an important data set for the prediction and validation of elastic properties of graphite-based materials. Previous results[3–7] have been obtained exclusively on pyrolytic graphite, for which the crystalline a axis is randomly oriented around a well-aligned (typically a few tenth of a degree) c axis. In particular, the results for C_{11}, C_{44}, and C_{13} show a large spread, which might be explained by the defect structure of the material. From a theoretical point of view graphite presents a major challenge as well due to the two completely different types of interatomic bonding: an exceptionally strong sp^2 covalent intralayer bonding and a weak van der Waals interlayer bonding. Again, different *ab initio* studies suffer from a significant spread in the elastic moduli.

Here we present the experimental determination of the five independent elastic moduli of single-crystalline graphite, using inelastic x-ray scattering (IXS). IXS overcomes the intrinsic difficulties of inelastic neutron scattering (INS)—namely, sample size and energy transfer limitations—and, compared to ultrasonic methods, is not sensitive to the defect structure of the material; we should mention that the first experimental determination of the optical phonons in the entire in-plane Brillouin zone of graphite was performed by IXS.[8] The moduli are obtained via the sound velocities V, as derived from the initial slope of the acoustic phonon branches along specific (mostly high-symmetry) directions, and Christoffel's equation.[9] The IXS experiment was performed on beamline ID28 at the European Synchrotron Radiation Facility. The instrument was operated at 17794 eV and provided an overall energy resolution of 3.0 meV full width at half-maximum (FWHM). The dimensions of the focused x-ray beam were 250×60 μm^2 (horizontal $\times$ vertical, FWHM). The direction and size of the momentum transfer were selected by an appropriate choice of the scattering angle and the sample orientation in the horizontal scattering plane. The momentum resolution was set to 0.2 nm^{-1} and 0.7 nm^{-1} in the horizontal and vertical planes, respectively. Further details of the experimental setup can be found elsewhere.[10] The investigated kish graphite samples were platelets consisting of single-crystalline regions with misaligned c axis oriented normal to the platelet. The intensity of disorder-induced Raman modes, linked to the relative defect concentration, indicates a very low defect density. The typical size of a single grain was about 0.8 mm in the lateral direction and 0.1 mm along the c axis. Thanks to the small beam dimensions individual domains with a mosaic spread of $\sim0.05°$ FWHM [for the (1 1 0) and (0 0 4) reflections] could be selected. The determined lattice parameters $a=2.463$ Å and $c=6.712$ Å are in excellent agreement with previous neutron diffraction results ($a=2.464$ Å and $c=6.711$ Å).[11]

In Fig. 1 we report examples of the collected IXS spectra. These are characterized by an elastic contribution centered at zero energy and two symmetric features: the Stokes and anti-Stokes peaks of the graphite acoustic phonons. The energy position $E(q)$ of the phonons was extracted using a model function composed of a sum of Lorentzian functions, for which the inelastic contributions were constrained by the Bose factor. This model function was convoluted with the experimentally determined resolution function and fitted to the IXS spectra, utilizing a standard χ^2 minimization routine. Typically, three to five q points along a specific crystallographic direction were used to extract the sound velocity; several pairs of phonon branches, associated with the same elastic modulus, are treated together. The sound velocity was

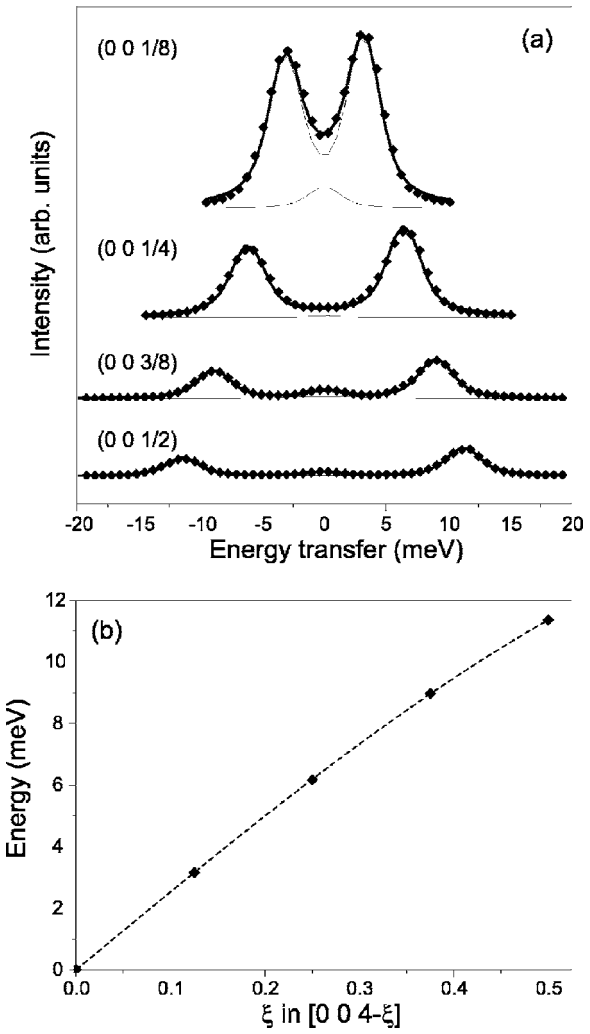

FIG. 1. (a) Selected IXS spectra for the LA [0 0 1] branch at the indicated q values (given in reciprocal lattice vector units). The experimental data are shown together with the best-fit results (thin solid lines for the individual components and thick solid lines for the total fit). The spectra are shifted along the vertical direction for clarity, conserving the same intensity scale. The counting time per point was 40 s. (b) Corresponding phonon dispersion; experimental points (solid diamonds) are given together with the best fit (dashed line).

derived from the slope of the acoustic phonon dispersion in the low-q limit, in most cases by a linear or a sinusoidal fit $E(q)=A\sin(\pi q/B)$, formally equivalent to limiting the interatomic interactions to nearest neighbors (A and B denote constants). However, due to the layered nature of graphite and, consequently, the high elastic anisotropy, transverse acoustic phonons with c-axis polarization, propagating in the a-b plane, $\mathrm{TA}[100]_{\langle 001\rangle}$ (here and below, if necessary, the polarization vector is indicated as a subscript), display a parabolic dispersion at low q: $\omega^2=Cq^2+Dq^4$, where C and D are constants, and the slope at $q=0$ is given by $\sqrt{C}$.[12] A further consequence of the high anisotropy of graphite is the need to take into account the effect of the finite momentum transfer, defined by the angular opening of analyzers. For this we have used the approximate IXS scattering factors, $S_j(\theta)$,

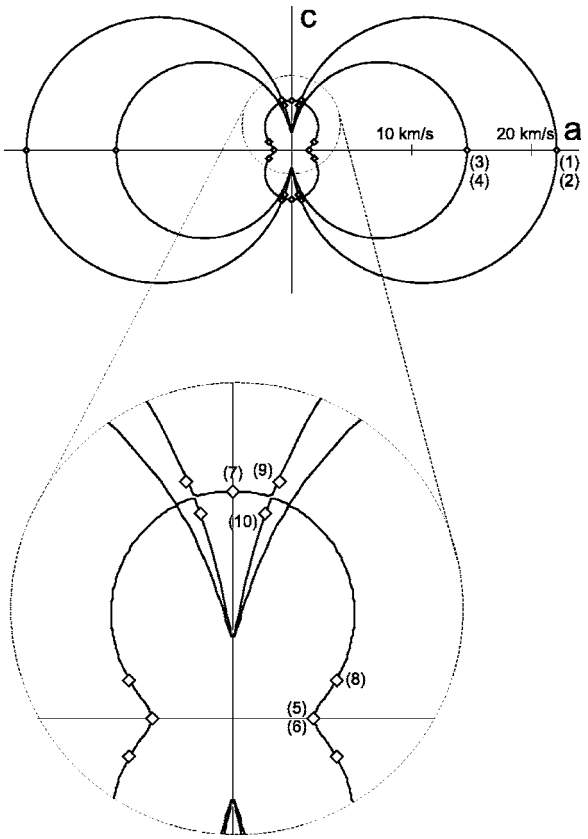

FIG. 2. Polar plot of the derived sound velocity data in the a-c plane: experimental data (diamonds) and fit results (solid lines). On the bottom an enlarged view of the low-velocity part is shown. Experimental points are enumerated as given in Table I.

calculated in the low-q limit: $S_j(\theta)\propto|\hat{e}_j(\theta)\cdot\vec{Q}|^2$. Here, $\hat{e}_j(\theta)$ denotes the phonon polarization vector and θ the angle with respect to the basal a-b plane; the momentum transfer $\vec{Q}$ ($\vec{Q}=\vec{q}+\vec{\tau}$, $\vec{q}$ the reduced momentum transfer vector, $\vec{\tau}$ the nearest reciprocal lattice vector) is directed towards the corresponding Γ point. Further details on finite-Q-resolution effects and their correction can be found in a previous work on the elasticity of hexagonal BN.[13]

Table I provides the list of investigated phonon branches and the corresponding derived sound velocities. The set of elastic moduli, calculated in a self-consistent manner on the basis of our experimental observations, is reported in Table II, and the fitted sound velocities are presented in a polar plot in Fig. 2. Apart from C_{13} all other elastic moduli can be calculated directly from a single sound velocity—i.e., $C_{11}=\rho V(\mathrm{LA}[100])^2$, $C_{66}=\rho V(\mathrm{TA}[100]_{\langle 1\text{–}20\rangle})^2$, $C_{44}=\rho V(\mathrm{TA}[110]_{\langle 001\rangle})^2=\rho V(\mathrm{TA}[001])^2$, and $C_{33}=\rho V(\mathrm{LA}[001])^2$, where ρ is the density. C_{13} contributes to the sound velocity only for nonpure directions (i.e., neither in the equatorial plane nor along the axial direction). Based on the results for C_{11}, C_{66}, C_{44}, and C_{33}, the most favorable direction with the largest $|dV/dC_{13}|$ occurs for $\theta\sim 10°$, and the phonon dispersion was therefore determined along the $\langle 1\ 1\ 35\rangle$ and $\langle 1\ 1\ 28\rangle$ directions. A numerical simulation of the scattered intensities based on the elastic moduli revealed

TABLE I. Summary of the investigated acoustic branches, indicating the direction of the total momentum transfer Q, the propagation and polarization vector of the phonon, and the derived apparent sound velocity. The parameter ξ is always positive; polarization vectors for quasilongitudinal (q-LA) and quasitransverse (q-TA) phonon branches are not indicated.

Notation	Momentum transfer	Propagation vector	Polarization vector	Velocity [km/s]
(1) LA[1 0 0]	[1+ξ 0 0]	[1 0 0]	⟨1 0 0⟩	22.16(17)
(2) LA⟨1 1 0⟩	[1+ξ 1+ξ 0]	[1 1 0]	⟨1 1 0⟩	
(3) TA[1 0 0]$_{\langle 1-20\rangle}$	[1−ξ 1+ξ 0]	[1 −1 0]	⟨1 1 0⟩	14.66(15)
(4) TA[1 1 0]$_{\langle 1-10\rangle}$	[1−2ξ 1+ξ 0]	[−2 1 0]	⟨0 1 0⟩	
(5) TA[1 1 0]$_{\langle 001\rangle}$	[1−ξ 1−ξ 2]	[1 1 0]	⟨0 0 1⟩	1.48(6)
(6) TA[1 0 0]$_{\langle 001\rangle}$	[1−ξ 0 3]	[1 0 0]	⟨0 0 1⟩	
(7) LA[0 0 1]	[0 0 4−ξ]	[0 0 1]	⟨0 0 1⟩	4.14(4)
(8) q-TA[1 1 2]	[1+ξ 1+ξ 2+2ξ]	[1 1 2]		2.02(2)
(9) q-LA[1 1 28]	[1+ξ 1+ξ 2+28ξ]	[1 1 28]		4.40(6)
(10) q-TA[1 1 35]	[1+ξ 1+ξ 2+35ξ]	[1 1 35]		3.77(4)

that a correction of +3% has to be applied to the determined sound velocity along the ⟨1 1 28⟩ direction.

C_{13} is poorly defined due to the very large structural anisotropy, but we can conclude that it is quite close to zero. C_{11} is slightly higher than determined by ultrasonic measurements,[5–7] most likely due to sensitivity of macroscopic methods to the presence of defects. At the same time our value is substantially lower than the one determined by INS for pyrolytic graphite.[3] The authors of the INS work were aware that the in-plane LA branch was the least reliable in this experiment due to the nature of the sample. The available value for the bulk modulus obtained by x-ray diffraction (XRD) from a polycrystalline sample[14] is very close to theoretical predictions and our result. Compared to hexagonal BN,[13] all the elastic moduli are systematically higher except for C_{44}, which is significantly lower for graphite. Such a difference can be explained by the additional electrostatic interaction between BN layers.

Numerous *ab initio* calculations within the local density approximation give a quite large spread of values.[15–18] Our data are in remarkable agreement with the those of Boettger,[15] which employed an all-electron, full-potential linear combination of Gaussian-type orbitals fitting-function technique.

The elasticity of graphite is directly linked to the mechanical properties of nanotubes. Our value of C_{11} =1.1 TPa provides the upper estimate of the on-axis Young's modulus of homogeneous carbon nanotubes. Experimental values for the single-walled nanotube (SWNT) Young's modulus vary from 1.0 (Ref. 19) to 1.25–1.28 TPa.[20,21] We

TABLE II. Comparison of our results with previous experiments and calculations. All values are in GPa.

	C_{11}	C_{12}	C_{13}	C_{33}	C_{44}	C_{66}	B
Present expt.	1109(16)	139(36)	0(3)	38.7(7)	5.0(3)	485(10)	36.4(11)
Previous expt.	1440(200)[a] 1060(20)[d]	180(20)[d]	15(5)[d] −51(6)[d]	37.1(5)[a] 36.5(10)[d]	4.6(2)[a] 5.05(35)[b] 4.0(4)[d]	460[a] 440(20)[d]	33.8(30)[c]
Theory	$C_{11}+C_{12}$=1280[e], $C_{11}+C_{12}$=1283, 976, 1235, 1230[f] 1118, 1079[e]	 235, 217[f]	−0.5[e] −2.8, −0.46, −4.6[g]	40.8[e] 29, 2.4, 1.9, 45, 29.5, 42.2[g] 0.8, 30.4[h]	4.5, 3.9[f]		38.3[e] 28.7[f] 27.8, 2.4 1.9, 41.2[g]

[a]INS (Ref. 3).
[b]Brillouin light scattering (Ref. 4).
[c]XRD (Ref. 14).
[d]Ultrasonic+sonic resonance+static test (Refs. 5–7).
[e]*Ab initio* calculations (Ref. 15).
[f]*Ab initio* calculations (Ref. 16).
[g]*Ab initio* calculation (Ref. 17).
[h]*Ab initio* calculation (Ref. 18).

would like to point out that the experimental values for BN nanotubes 1.22 ± 0.24 TPa (Ref. 22) are also overestimated compared to our evaluations [0.8 TPa (Ref. 13)]. Recent calculations[23,24] provide values of 1.09 TPa and 1.22 TPa for (6,6) nanotubes using *ab initio* methods or a tight-binding scheme, respectively. We believe that our estimates provide a solid background for both theoretical modeling and analysis of experimental data. It must be noted that when a ropelike close-packed configuration is considered, a packing factor must be taken into account, which yields for (10,10) SWNTs a decrease of Young's modulus E by a factor ~ 1.7—i.e., from 1.1 TPa to 0.64 TPa. Thus, the ultimate tensile strength of a (crystalline) SWNT rope can be estimated as $\sigma_T \sim 0.1E \sim 60-70$ GPa.

[1] S. Iijima, Nature (London) **354**, 56 (1991).
[2] S. Stankovich, D. Dikin, G. Dommett, K. Kohlhaas, E. Zimney, E. Stach, R. Piner, S. Nguyen, and R. Ruoff, Nature (London) **442**, 282 (2006).
[3] R. Nicklow, N. Wakabayashi, and H. G. Smith, Phys. Rev. B **5**, 4951 (1972).
[4] M. Grimsditch, J. Phys. C **16**, L143 (1983).
[5] E. J. Seldin and C. W. Nezbeda, J. Appl. Phys. **41**, 3389 (1970).
[6] G. B. Spence and E. J. Seldin, J. Appl. Phys. **41**, 3383 (1970).
[7] H. J. F. Jansen and A. J. Freeman, Phys. Rev. B **35**, 8207 (1983).
[8] J. Maultzsch, S. Reich, C. Thomsen, H. Requardt, and P. Ordejón, Phys. Rev. Lett. **92**, 075501 (2004).
[9] B. A. Auld, *Acoustic Fields and Waves in Solids* (Wiley, New York, 1973), Vol. 1.
[10] M. Krisch, J. Raman Spectrosc. **34**, 628 (2003).
[11] P. Trucano and R. Chen, Nature (London) **258**, 136 (1975).
[12] H. Zabel, J. Phys.: Condens. Matter **13**, 7679 (2001).
[13] A. Bosak, J. Serrano, M. Krisch, K. Watanabe, T. Taniguchi, and H. Kanda, Phys. Rev. B **73**, 041402(R) (2006).
[14] M. Hanfland, H. Beister, and K. Syassen, Phys. Rev. B **39**, 12598 (1989).
[15] J. C. Boettger, Phys. Rev. B **55**, 11202 (1997).
[16] T. Tohei, A. Kuwabara, F. Oba, and I. Tanaka, Phys. Rev. B **73**, 064304 (2006).
[17] N. Mounet and N. Marzari, Phys. Rev. B **71**, 205214 (2005).
[18] M. Hasegawa and K. Nishidate, Phys. Rev. B **70**, 205431 (2004).
[19] M.-F. Yu, B. S. Files, S. Arepalli, and R. S. Ruoff, Phys. Rev. Lett. **84**, 5552 (2000).
[20] E. W. Wong, P. E. Sheehan, and C. M. Lieber, Science **277**, 1971 (1997).
[21] A. Krishnan, E. Dujardin, T. W. Ebbesen, P. N. Yianilos, and M. M. J. Treacy, Phys. Rev. B **58**, 14013 (1998).
[22] N. G. Chopra and A. Zettl, Solid State Commun. **105**, 297 (1998).
[23] D. Sánchez-Portal, E. Artacho, J. M. Soler, A. Rubio, and P. Ordejón, Phys. Rev. B **59**, 12678 (1999).
[24] E. Hernández, C. Goze, P. Bernier, and A. Rubio, Phys. Rev. Lett. **80**, 4502 (1998).